

Quantitative analysis of dinuclear manganese(II) EPR spectra

Adina P. Golombek and Michael P. Hendrich*

Department of Chemistry, Carnegie Mellon University, 4400 Fifth Ave., Pittsburgh, PA 15213, USA

Received 21 April 2003; revised 25 July 2003

Communicated by Arthur Schweiger

Abstract

A quantitative method for the analysis of EPR spectra from dinuclear Mn(II) complexes is presented. The complex $[(\text{Me}_3\text{TACN})_2\text{Mn}(\text{II})_2(\mu\text{-OAc})_3]\text{BPh}_4$ (**1**) ($\text{Me}_3\text{TACN} = N, N', N''$ -trimethyl-1,4,7-triazacyclononane; $\text{OAc} = \text{acetate}^{1-}$; $\text{BPh}_4 = \text{tetraphenylborate}^{1-}$) was studied with EPR spectroscopy at X- and Q-band frequencies, for both perpendicular and parallel polarizations of the microwave field, and with variable temperature (2–50 K). Complex **1** is an antiferromagnetically coupled dimer which shows signals from all excited spin manifolds, $S = 1$ to 5. The spectra were simulated with diagonalization of the full spin Hamiltonian which includes the Zeeman and zero-field splittings of the individual manganese sites within the dimer, the exchange and dipolar coupling between the two manganese sites of the dimer, and the nuclear hyperfine coupling for each manganese ion. All possible transitions for all spin manifolds were simulated, with the intensities determined from the calculated probability of each transition. In addition, the non-uniform broadening of all resonances was quantitatively predicted using a lineshape model based on D - and r -strain. As the temperature is increased from 2 K, an 11-line hyperfine pattern characteristic of dinuclear Mn(II) is first observed from the $S = 3$ manifold. D - and r -strain are the dominate broadening effects that determine where the hyperfine pattern will be resolved. A single unique parameter set was found to simulate all spectra arising for all temperatures, microwave frequencies, and microwave modes. The simulations are quantitative, allowing for the first time the determination of species concentrations directly from EPR spectra. Thus, this work describes the first method for the quantitative characterization of EPR spectra of dinuclear manganese centers in model complexes and proteins. The exchange coupling parameter J for complex **1** was determined ($J = -1.5 \pm 0.3 \text{ cm}^{-1}$; $H_{\text{ex}} = -2JS_1 \cdot S_2$) and found to be in agreement with a previous determination from magnetization. The phenomenon of exchange striction was found to be insignificant for **1**.

© 2003 Elsevier Inc. All rights reserved.

Keywords: Quantitative EPR simulation; Dinuclear Mn(II); D -strain; r -strain; Q-band; Parallel mode

1. Introduction¹

Dinuclear manganese centers have been identified in such proteins as catalases [1,2], arginase [3,4], thiosulfate oxidase [5], dinitrogen reductase regulatory protein [6], aminopeptidases [7,8] and λ protein phosphatase [9]. In addition, several dimanganese-substituted proteins have

also been prepared, such as ribonucleotide reductase [10,11], phosphotriesterase [12], concanavallin A [13], and various enolases [14], in attempts to model structural or functional properties, or to probe the active site with a spectroscopically active metal. The two manganese ions are usually bridged by one or more carboxylate groups from the protein, and/or water or hydroxide. The remainder of the manganese coordination is O- or N-donors from protein residues and water. All these proteins, with the exception of catalase, are found to be stable and function with specifically the divalent state of both manganese ions. Manganese catalases have four accessible oxidation states, and the active state of the protein is believed to cycle between the $\text{Mn}_2(\text{II},\text{II})$ and $\text{Mn}_2(\text{III},\text{III})$ oxidation states [15–19].

* Corresponding author. Fax: 1-412-268-1061.

E-mail address: hendrich@andrew.cmu.edu (M.P. Hendrich).

¹ Abbreviations: EPR, electron paramagnetic resonance; EXAFS, extended X-ray absorption fine structure; Me_3TACN , N, N', N'' -trimethyl-1,4,7-triazacyclononane; OAc , acetate; BPh_4 , tetraphenylborate¹⁻; $\text{DMF} = N, N$ -dimethylformamide; NEt_3 , tetraethylamine¹⁺; salm , 2-(bis(salicylideneamino)methyl)phenolate³⁻; EDTA, ethylenediaminetetraacetic acid; ICP, inductively coupled plasma.

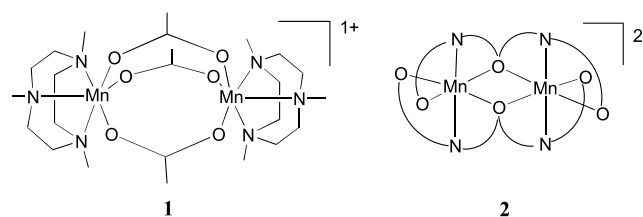
The two main spectroscopic tools used for the characterization of manganese proteins are EPR and EXAFS spectroscopies. Dinuclear Mn(II) centers are often identified by observation of a characteristic 11-line hyperfine pattern in EPR spectra. However, the origin of the pattern is uncertain and it is not observed for all dinuclear Mn centers. EPR spectroscopic characterization of dimanganese clusters has long relied on a qualitative understanding of the positions of a few resonances from what is typically an exceedingly complicated spectrum. Consequently, although much has been learned from such studies, proof of correct spectral assignment and the ability to determine species concentrations has not been possible. Characterization of Mn clusters with higher nuclearity, such as the oxygen evolving Mn cluster of photosystem II, also relies on EPR spectroscopy to identify properties of the clusters. While systems with Mn nuclearity greater than 2 are outside of the scope of the present work, a quantitative treatment of mono- and dinuclear Mn centers is also an important step for an understanding of more complicated systems.

The first manganese dimers to be studied by EPR spectroscopy were pairs produced as substitutional impurities in various diamagnetic host lattices [20–23]. These magnetically dilute single crystal systems allowed for the observation of distinct lines arising from each of the many transitions. The number and positions of these lines changed for various orientations of the crystals relative to the external magnetic field. Exchange coupling constants were determined through studies of the temperature dependence of the signals. Zero-field splittings and dipolar coupling parameters could be uniquely determined from the field positions of the resonances observed at various spectrometer frequencies [24]. One such study provided a simulation of the observed spectrum, in which each spin manifold was considered to have an independent set of zero-field splitting parameters [21]. Although much more information can be derived from spectroscopy of single crystals, magnetically dilute crystals are not readily available and thus studies of powders or frozen solutions are much more common.

The spectra arising from manganese dimers in solution are much more difficult to interpret than those of single crystals, owing to the random distribution of molecular orientations. Spectra have been identified as arising from dimer systems by their dissimilarity to the spectra of monomeric analogues [25], their similarity to other dimer spectra [26], or more definitively, by their characteristic 11-line hyperfine pattern with a splitting of 4.0–4.7 mT [27–31]. More detailed studies of Mn(II) dimer EPR spectra have attempted to deconvolute the experimental spectra at low temperatures into two base spectra arising from the $S = 1$ and 2 spin manifolds using single-valued decomposition [32,33]. The temperature dependence of the base spectra has been used to

determine the exchange coupling parameter J . The base spectra have also been used to determine the effective D -value of one spin manifold, usually believed to be $S = 2$, by comparisons of some of the experimentally observed spectral line positions to those predicted theoretically. Early attempts at simulation of spectra of manganese dimers in solution have yielded approximate agreement to a limited part of the experimental data [34]. More recently, the $S = 2$ manifold of a synthetic manganese dimer was simulated with the inclusion of hyperfine splittings [35]. These early simulation attempts have generally focused on line positions of the $S = 1$ or 2 spin manifolds and assumed axial symmetry. Although in some cases transition probabilities have been calculated, a quantitative match to spectral intensities has not been attempted and the treatment of lineshapes is phenomenological.

Synthetic model systems are more easily characterized than protein active sites and are helpful in understanding the active sites of proteins. Many synthetic complexes which model aspects of the protein metal sites have also been characterized in various oxidation states [36–38]. Complex **1** studied here is a Mn(II) dimer in which the two manganese centers are antiferromagnetically exchange coupled through three bridging acetate groups. The remainder of the metal coordination is composed of nitrogen donors from the tridentate ligand N, N', N'' -trimethyl-1,4,7-triazacyclononane (Me_3TACN), thus providing donor atoms similar to those found in proteins. The Mn(II) dimer complex has been characterized by X-ray crystallography [38,39] and possesses approximate D_{3h} symmetry, with a C_3 -axis along the Mn–Mn vector and a mirror plane relating the two halves of the dimer to each other.



The exchange coupling between the Mn(II) ions was previously determined by magnetometry to be $J = -1.7(1) \text{ cm}^{-1}$ ($H_{\text{ex}} = -2JS_1 \cdot S_2$). Thus, this complex is well suited for a proof of principle in the quantitative characterization of dinuclear Mn(II) complexes with EPR spectroscopy.

Low temperature EPR spectra and accompanying simulations of a second synthetic Mn(II) dimer complex **2** are also presented. This dimer has two phenoxide bridges and terminal oxygen and nitrogen ligation from its two Schiff base chelating ligands, 2-(bis(salicylideneamino)methyl)phenolate³⁻ (salmp).

In recent work, we have demonstrated the ability to quantitatively analyze spectra of mononuclear Mn(II)

proteins [11]. Here, we present advances in spectral analysis using new simulation software which for the first time enables a quantitative treatment of the EPR spectra of Mn(II) dimers through the simulation of their spectra using a single unique parameter set. The approach uses data from two microwave frequencies, various temperatures, and two polarization directions of the microwave magnetic field to determine a unique spin Hamiltonian which simultaneously fits all the EPR spectra obtained under these various conditions. The simulations treat all aspects of the spectra with a quantitative physical model. From a single parameter set, all resonance positions and signal intensities are determined, and all linewidths are determined from molecular parameters rather than phenomenological parameters. Importantly, this now allows the determination of the concentration of species in a sample.

The task of assigning spectral features is simpler at higher microwave frequencies where $h\nu \gg D$. However, the ability to analyze more complicated X-band (9 GHz) data is important for various reasons: (1) most instruments available to researchers are X-band spectrometers; (2) signal sensitivity is significantly better at lower frequency and detection of protein signals is difficult at and above Q-band (35 GHz) frequencies; and (3) multiple frequencies provide additional information and extra constraints to ensure that a unique parameter set is determined.

2. Analysis of experimental spectra

The EPR spectra of a coupled dimer system can be described with the spin Hamiltonian [40]:

$$H = -2JS_1 \cdot S_2 + H_{\text{dip}} + H_1 + H_2, \quad (1)$$

where J is the isotropic exchange coupling constant for coupling between the two Mn(II) ions of the dimer, H_{dip} is the dipolar interaction between the two Mn(II) spin centers, and H_i ($i = 1, 2$) are the spin Hamiltonians corresponding to each individual Mn(II) ion. The dipolar spin–spin Hamiltonian is

$$H_{\text{dip}} = \frac{\mu_0}{4\pi} \beta^2 \left[\frac{(\mathbf{S}_1 \cdot \mathbf{g}_1) \cdot (\mathbf{S}_2 \cdot \mathbf{g}_2)}{r^3} - \frac{3(\mathbf{S}_1 \cdot \mathbf{g}_1 \cdot \mathbf{s})(\mathbf{S}_2 \cdot \mathbf{g}_2 \cdot \mathbf{r})}{r^5} \right] = \mathbf{S}_1 \cdot \mathbf{D}_{12} \cdot \mathbf{S}_2, \quad (2)$$

where \mathbf{r} is the internuclear vector between the two manganese ions as defined in Fig. 1. The dipolar term is calculated using the distance between the two manganese centers (r) and the dipolar angles (θ_r, ϕ_r) between the coordinate systems of the Mn(II) atoms. The dipolar expression can be written in an equivalent tensor form where the components of \mathbf{D}_{12} are obtained from Eq. (2) [41]. The spin Hamiltonians of the Mn(II) spin centers are

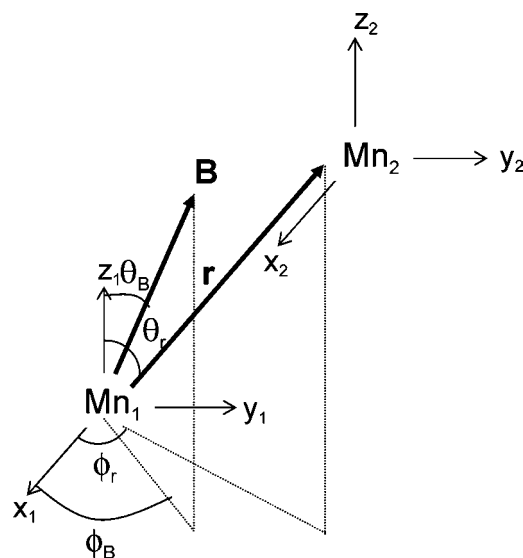


Fig. 1. Definition of the principle axis systems for the Mn sites of the orientations of the dipolar vector (\mathbf{r}) and magnetic field (\mathbf{B}).

$$H_i = \beta \mathbf{B} \cdot \mathbf{g}_i \cdot \mathbf{S}_i + \mathbf{S}_i \cdot \mathbf{D}_i \cdot \mathbf{S}_i + \mathbf{S}_i \cdot \mathbf{A}_i \cdot \mathbf{I}_i, \quad i = 1, 2, \quad (3)$$

where \mathbf{g}_i , \mathbf{D}_i , and \mathbf{A}_i are the electronic Zeeman, zero-field splitting, and nuclear hyperfine tensors, respectively, for each manganese ion with electronic spin \mathbf{S}_i . For Mn(II) dimers, the electron and nuclear spin of each Mn(II) ion is $S_i = 5/2$ and $I_i = 5/2$, respectively.

Mn(II) ions have a singlet orbital ground state (6A), with the first excited orbital state (4T) more than $10,000 \text{ cm}^{-1}$ above the ground state. Consequently, the zero-field energies of Mn(II) ions are generally small, $D_i < 0.1 \text{ cm}^{-1}$ [42,43]. For manganese dimeric complexes, the bridging atoms typically give a Mn–Mn exchange interaction which is significantly larger than 0.1 cm^{-1} . In this strong exchange regime, the isotropic exchange coupling energy is much larger than the electronic Zeeman energy ($|J| \gg g\beta B$) and the zero-field splitting ($|J| \gg D_i$). The dimer system may then be regarded as a ladder of isolated spin manifolds. These spin manifolds have total spin quantum numbers of $S = 0, 1, 2, 3, 4$, and 5 , each with a degeneracy of $(2S + 1)$. The separation between the spin manifolds is much larger than the microwave energy ($h\nu$) at X- and Q-band frequencies and no transitions are observable between spin manifolds. The individual spin manifolds can be considered independently and their corresponding spectra can be simulated using a spin Hamiltonian for each individual spin manifold given by [44]

$$H_S = \beta \mathbf{B} \cdot \mathbf{g}_S \cdot \mathbf{S} + \mathbf{S} \cdot \mathbf{D}_S \cdot \mathbf{S} + \mathbf{I} \cdot \mathbf{A}_S \cdot \mathbf{S}, \quad (4)$$

where \mathbf{g}_S , \mathbf{D}_S , and \mathbf{A}_S are the electronic Zeeman, zero-field splitting, and nuclear hyperfine tensors, respectively, of the spin manifolds of the coupled system, and \mathbf{S} is the spin operator of the coupled spin manifolds. The parameters of the coupled spin system can be expressed

as linear combinations of the parameters of the individual spin centers. For the manganese dimer systems studied here these relationships are:

$$\mathbf{g}_S = \frac{1}{2}\mathbf{g}_1 + \frac{1}{2}\mathbf{g}_2, \quad (5)$$

$$\mathbf{D}_S = d_1\mathbf{D}_1 + d_2\mathbf{D}_2 + d_{12}\mathbf{D}_{12}, \quad (6)$$

$$\mathbf{A}_S^{\text{Mn}_i} = \frac{1}{2}\mathbf{A}_{\text{Mn}_i}, \quad (7)$$

where the coefficients d_1 , d_2 , and d_{12} are specific to the particular spin manifold and have been tabulated elsewhere [44]. For Mn(II) ions, the contributions from spin–orbit coupling to the g_i -tensor and hyperfine tensor are small, thus we will assume that both tensors g_i and A_i are isotropic and $g_i = 2.0$. In the complex studied here, the two manganese centers of the dimer have identical ligation. The coordination geometry of one manganese ion is related to the other by a mirror plane, thus, we assume $g_1 = g_2 = 2.0$, $A_1 = A_2$, and $\mathbf{D}_1 = \mathbf{D}_2$.

The simulations are calculated by diagonalizing the spin Hamiltonian of Eq. (4) for each spin manifold in accordance with Eqs. (5)–(7). This significantly reduces the calculation time; however, the slower full diagonalization of Eq. (1) is also performed as a check of the results. The nuclear hyperfine interaction is treated with second-order perturbation theory. The powder lineshape of a specified doublet is generated for a uniform spherical distribution of the magnetic-field vector \mathbf{B} . For reviews of powder lineshape simulations for EPR spectroscopy see references [40,45]. The simulations for all significantly populated spin manifolds S include all possible transitions for θ_B , ϕ_B spanning a hemisphere (see Fig. 1). The intensities are calculated from the square of the transition moment using the eigenfunctions given by the diagonalization. The simulations are generated on a 1 GHz PC compatible computer.

We will show that the spectral lineshapes are determined by a combination of D -strain, r -strain, and unresolved hyperfine splittings. Small variations in metal–ligand coordination may result in a distribution of orbital energy levels, and in turn, a distribution in the zero-field splittings, referred to as D -strain [46]. Variation in the metal–metal distance (r) results from similar disorder in the molecular structure, and the consequent variation of the magnetic dipole–dipole energy between Mn(II) ions causes a distribution in spin energies. This is referred to as r -strain and will affect spectra differently than D -strain. We assume that these parameter variations can be modeled with a Gaussian distribution in the parameters D , E/D , and r , specified as one standard deviation, σ_D , $\sigma_{E/D}$, and σ_r , respectively. A residual linewidth of σ_B in the magnetic field is also specified to account for other unspecified lineshape determinants such as unresolved hyperfine from coordinated nitrogen to Mn(II). Gaussian spin-packets with linewidths

determined in relation to these linewidth parameters (σ_D , $\sigma_{E/D}$, σ_r , and σ_B) and properly normalized for field-swept experimental spectra are folded into the spectrum at each resonance position. Our treatment of the lineshape is based on the physical description of the spin system given by Eq. (1), using molecular linewidth parameters, rather than on the common practice of phenomenological linewidths in the magnetic field.

The simulations are generated with careful consideration of all intensity factors, both theoretical and instrumental, to allow direct scaling of spectra to sample concentrations. The only unknown variable relating spin concentration to signal intensity is an instrumental factor that depends on the microwave detection system. However, this factor is determined by a spin standard, CuEDTA, for which the copper concentration was accurately determined by ICP spectroscopy.

A least squares fitting routine was used to simultaneously match up to four spectra recorded under various conditions, while varying one or more of the spectral parameters within a specified range of reasonable values. The approach to simulating the observed EPR signals began with achieving correct simulations of spectra at low temperature from the $S = 1$ manifold at both frequencies and polarizations of the magnetic field. Complexity was added by then including higher excited states into the data fit, thus narrowing the possible solutions. Both perpendicular and parallel mode spectra from the X- and Q-band frequencies were fit in order to simultaneously fit multiple features in all of these spectra. The best possible parameter sets from these simulations were used as starting points to match features of higher excited spin manifold spectra. More complicated spectra recorded at higher temperatures in which multiple excited spin manifolds were populated were added to the set used by the fitting routine until a good match was found to all excited spin manifolds in both parallel and perpendicular modes, and at both X- and Q-band frequencies.

The parameter D_{Mn} was varied over the range 0.01–10 cm⁻¹, $E_{\text{Mn}}/D_{\text{Mn}}$ was allowed to vary over the full range, and the dipolar angles were allowed to vary over the entire range of angular space. The distribution parameters $\sigma_{D_{\text{Mn}}}$ and $\sigma_{E_{\text{Mn}}/D_{\text{Mn}}}$ were linked to their parent parameters and allowed to vary over a range of one-quarter to one-half the values of D_{Mn} and $E_{\text{Mn}}/D_{\text{Mn}}$, respectively. Thus, an exhaustive range of parameter space was explored to arrive at the unique solutions described in Section 4.

3. Experimental methods

The complex [(CH₃)₃triazacyclononane]₂Mn(II)₂(μ-CH₃CO₂)₃(BPh₄) (**1**) was generously donated by Dr. Karl Wieghardt and Dr. Thomas Weyhermüller and prepared as described elsewhere [39]. The complex was

provided as crystalline material and EPR samples were prepared anaerobically in an Ar- or N₂-filled glovebox (Vacuum Atmospheres). Acetonitrile was dried over CaH₂ and degassed prior to introduction to the glovebox, and anhydrous *N,N*-dimethylformamide was obtained in a Sure/Seal bottle under an N₂ atmosphere (Aldrich) and used as received.

X-band EPR spectra were recorded on a Bruker ESP300 spectrometer equipped with an Oxford ESR910 cryostat for low temperature measurements and a bimodal cavity (Bruker ER4116DM) for generation of the microwave fields parallel ($B_1 \parallel B$) and perpendicular ($B_1 \perp B$) to the static field. Q-band EPR spectra were recorded on a Bruker spectrometer equipped with a low temperature immersion microwave probe and cryogenic system of our own construction which allows variable orientation of B_1 with respect to B [47]. The microwave bridge was modified with placement of a low-noise 20 dB amplifier (Quinstar Technology Inc. QLN3635) between the circulator and detection diode. For both instruments, the microwave frequency was calibrated with a frequency counter and the magnetic field with a gaussmeter. The sample temperature of the X-band cryostat was calibrated using a calibrated carbon-glass resistor (LakeShore CGR-1-1000) placed in an EPR tube to mimic a sample. The sample temperature in the Q-band cryostat was determined from calibrated sensors (carbon-glass, LakeShore CGR-1-1000), positioned above and below the sample cavity. All microwave data were recorded with nonsaturating microwave power. The modulation frequency for all X- and Q-band spectra was 100 kHz, except for Fig. 6d, where 3.1 kHz was used to improve signal-to-noise.

4. Results

4.1. Q-Band EPR Data of $[(Me_3TACN)_2Mn(II)_2(\mu-CH_3CO_2)_3](BPh_4)$ (**1**)

Fig. 2a shows the Q-band spectrum of **1** at 2 K (solid line) for $B_1 \perp B$, in which peaks are observed at $g = 2.6$, 2.3, and 1.8. The six-line hyperfine signal centered at $g = 2.0$ originates from a mononuclear Mn(II) impurity. The relative concentration of this species varies in different sample preparations and is less than 4% of the dimer concentration. Due to the inverse temperature dependence of this mononuclear Mn(II) signal, it interferes with the dimer signal only at the lowest temperatures. The spectrum of **1** at 2 K for $B_1 \parallel B$ (Fig. 3a) shows a derivative signal at $g = 4.1$. This signal has the same field position as a low field peak in the perpendicular mode spectrum (data not shown) and will be shown to arise from the same transition.

At 2 K, primarily the ground ($S = 0$) and first excited ($S = 1$) states are populated, with less than 0.1% of the

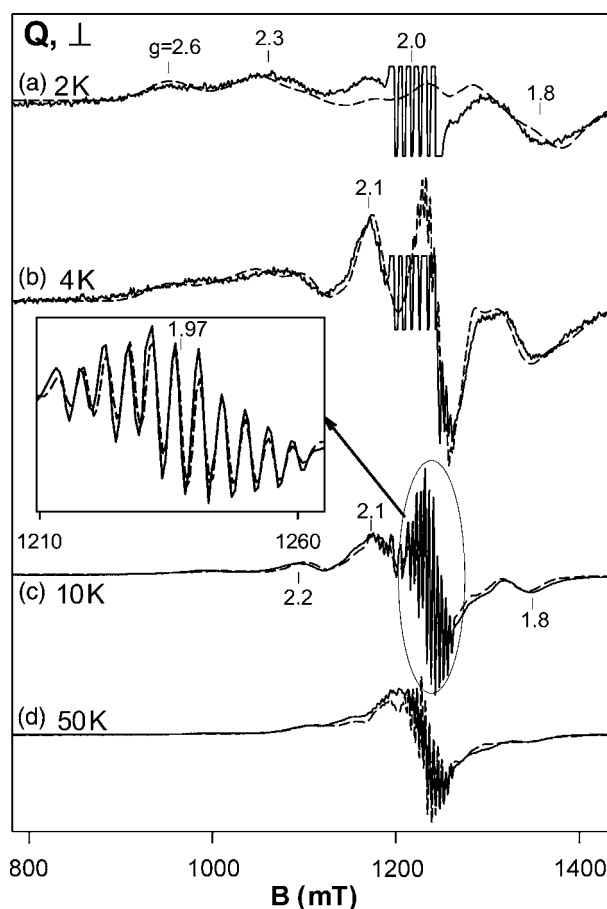


Fig. 2. Variable temperature, perpendicular mode, Q-band EPR spectra (solid lines) and simulations (dashed lines) of a 14 mM sample of $[(Me_3TACN)_2Mn(II)_2(\mu-CH_3CO_2)_3](BPh_4)$ (**1**) in 50:50 CH₃CN:DMF. The simulation parameters are given in Table 1. All spectra are plotted for normalized instrumental power, gain, and modulation; relative displayed intensities: (a) 5 \times ; (b) 2 \times ; (c,d) 1 \times . EPR conditions: temperatures as listed; frequency, 34.2 GHz; power, 0.9 μ W (a,b); 0.09 mW (c,d); $B_{mod} = 0.3$ mT_{pp}.

spin population in the second excited ($S = 2$) state, for $J = -1.7 \pm 0.1$ cm⁻¹ ($H_{ex} = -2JS_1 \cdot S_2$), determined previously by magnetization [39]. The ground state is EPR silent, thus the $S = 1$ state gives rise to the EPR signals at low temperature observed in both perpendicular and parallel modes. An energy level diagram (Fig. 4) shows the Q-band EPR transitions when the magnetic field is oriented along the molecular Z -axis. The $S = 1$ manifold has three possible transitions, all of which have significant intensity for various orientations of the magnetic field.

The assignment of features in these and the following spectra is based on the simulations (dashed lines) overlaid on the data. The parameters of the simulations are given in Table 1. The $\Delta M_S = \pm 2$ transition of the $S = 1$ manifold, between levels 2–4 in the energy level diagram (which will be written as 2|4), gives the low-field signal at $g = 4.1$ in both perpendicular and parallel modes. This signal is relatively sharp because its position does not

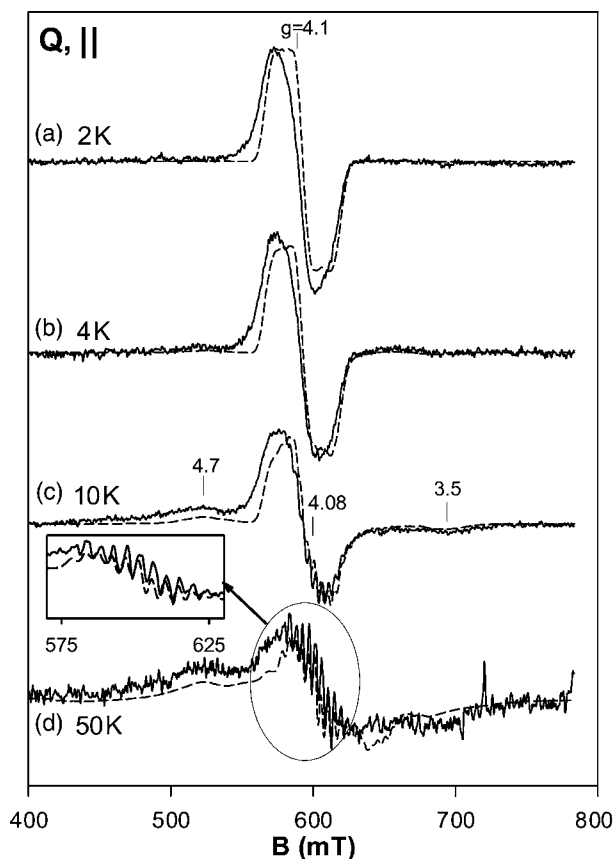


Fig. 3. Variable temperature, parallel mode, Q-band EPR spectra (solid lines) and simulations (dashed lines) of a 14 mM sample of **1** in 50:50 CH₃CN:DMF. The simulation parameters are given in Table 1. All spectra are plotted for normalized instrumental power, gain, and modulation; relative displayed intensities: (a,b) 1×; (c) 3×; (d) 20×. EPR conditions: temperatures as listed; frequency, 34.2 GHz; power, 0.009 mW (a); 0.09 mW (b,c); 0.9 mW (d); $B_{\text{mod}} = 0.3 \text{ mT}_{\text{pp}}$.

significantly depend on the orientation of the magnetic field. The signals at $g = (2.6, 1.8)$ and 2.3 are from the two $\Delta M_S = \pm 1$ transitions, $2|3$ and $3|4$, respectively, and are highly dependent on the orientation of the magnetic field.

Raising the temperature to 4 K causes noticeable changes in the EPR spectrum as the $S = 2$ manifold becomes populated, giving rise to a peak in the perpendicular mode spectrum at $g = 2.1$ (Fig. 2b). A second peak centered at $g = 1.96$ is partially obscured by the free Mn(II) signal at $g = 2$ while a third signal at $g = 1.8$ contributes to that already seen from the $S = 1$ manifold at the same field position. The $\Delta M_S = \pm 2$ transitions of the $S = 2$ manifold are only weakly allowed and contribute little intensity to the spectra in both perpendicular and parallel modes. These signals are at the same approximate resonance field as the $2|4$ transition of the $S = 1$ manifold but have much less intensity and so are not discernable. Thus, the parallel mode spectrum shown in Fig. 3b has not changed significantly from that seen at 2 K. Although the $S = 3$

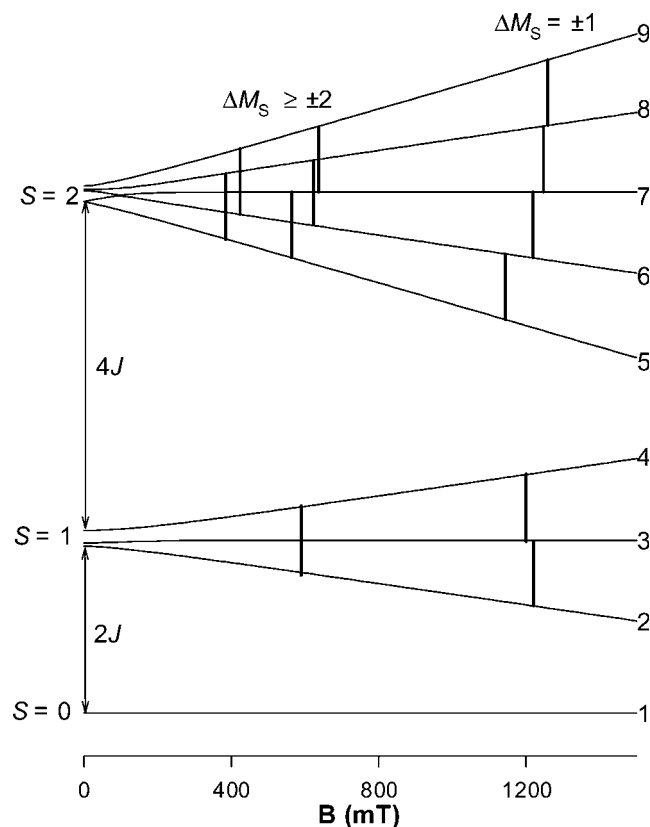


Fig. 4. The energies and transitions for the lowest three spin manifolds of **1** using the parameters given in Table 1. The magnetic field is along the Z-axis of the **D**-tensor ($\theta_B = 0^\circ$) and the bars are the observed Q-band EPR transitions.

Table 1
Parameters for the simulation of the EPR spectra of [(Me₃TACN)₂Mn(II)₂(μ-OAc)₃]BPh₄ (**1**) in pure DMF or pure CH₃CN^a

Parameter	DMF	CH ₃ CN
D_{Mn} (cm ⁻¹)	-0.0263	0.018 (-0.029)
$\sigma_{D_{\text{Mn}}}$ (cm ⁻¹)	0.01315	0.007
$E_{\text{Mn}}/D_{\text{Mn}}$	0.1043	0.737 (0.082)
$\sigma_{E_{\text{Mn}}/D_{\text{Mn}}}$	0.05215	0.290
r (Å)	4.034	4.034
σ_r (Å)	0.09	0
θ (°)	33	86 (40)
ϕ (°)	71	130 (6)
g	2	2
A (MHz)	250	250
J (cm ⁻¹)	-1.5	-1.7
σ_B (mT)	1	10

^a The parameters are listed as derived from the actual simulations. The conversion to the conventional reference frame where $0 < E/D < 1/3$ is given in parentheses when applicable. The parameters for pure DMF and 50/50 DMF/CH₃CN are the same.

manifold has less than 1% of the total spin population, the relative intensity of its signal is sufficiently large as to contribute hyperfine lines near $g = 2$ as discussed next.

Upon significant population of the $S = 3$ spin manifold at 10 K (Figs. 2c and 3c), intense hyperfine patterns

appear in the EPR spectra. The most prominent in the perpendicular mode spectrum is an 11-line pattern with spacings of approximately 4.6 mT centered at $g = 1.97$ which is matched by the simulation as shown in the inset of Fig. 2. This feature arises from a single transition within the $S = 3$ manifold (12|13), while the hyperfine lines of the other $\Delta M_S = \pm 1$ transitions are almost completely unresolved. The other features of the spectrum at $g = 2.2, 2.1,$ and 1.8 have contributions from the $S = 1, 2,$ and 3 spin manifolds. The more intense features of the $S = 2$ spectrum at $g = 2.08$ and 1.96 arise from the more isotropic transitions 6|7 and 7|8. The anisotropic transitions 5|6 and 8|9 produce the smaller peaks in the EPR spectrum.

A hyperfine pattern can also be observed in the parallel mode arising from the $S = 3$ manifold, which has a transition overlapping the $\Delta M_S = \pm 2$ transitions of the other spin manifolds at $g = 4.08$ (Fig. 3c). This hyperfine pattern also arises from a single $\Delta M_S = \pm 2$ transition (12|14) within the $S = 3$ manifold, while the other $\Delta M_S = \pm 2$ transitions give rise to more broadened peaks such as those at $g = 4.7$ and 3.5 . This hyperfine pattern is only resolved in parallel mode, and specifically not

resolved for the corresponding peak in the perpendicular mode spectrum.

The spectra of dinuclear manganese complexes become very complicated at higher temperatures because of overlapping signals from the $S = 2$ to 5 manifolds. To identify signals and their corresponding spin manifolds, Fig. 5 shows individual simulations of spectra for each of the five excited spin manifolds. As temperature is increased, the features which grow in from higher excited spin manifolds are not easily distinguishable. Fig. 2d shows the perpendicular mode spectrum of **1** at 50 K, which is centered around the hyperfine patterns at $g = 2.00$. The $\Delta M_S = \pm 2$ signal from $S = 1$ is overwhelmed by signals from more intense $\Delta M_S = \pm 1$ transitions of the higher spin manifolds. With all the excited spin manifolds ($S = 1$ to 5) populated at this temperature, the resultant spectrum has features which are less sharply defined. The highest three excited spin manifolds have spectral features in similar field positions (Fig. 5),

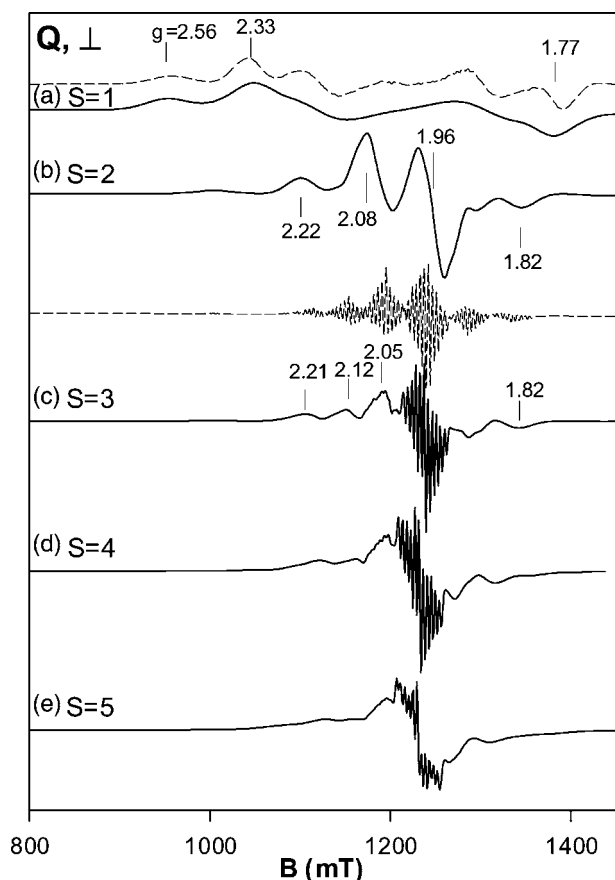


Fig. 5. Simulations of the individual spin manifolds $S = 1$ to 5 of complex **1** for $B_1 \perp B$, $T = 50$ K, frequency = 34.2 GHz. Simulation parameters are from Table 1. The relative displayed intensities are: (a) $50\times$; (b) $5\times$; (c–e) $1\times$. See text in Section 5.1 for explanation of dashed lines.

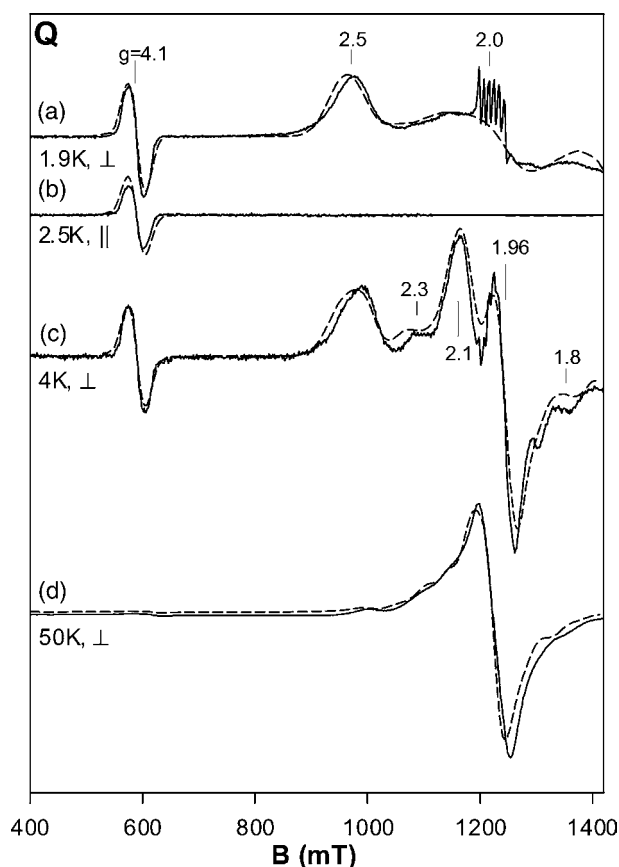


Fig. 6. Variable temperature perpendicular (a, c, and d) and parallel (b) mode Q-band EPR spectra (solid lines) and simulations (dashed lines) of a 21.3 mM sample of **1** in CH_3CN . The simulation parameters are given in Table 1. All spectra are plotted for normalized instrumental power, gain, and modulation; relative displayed intensities: (a–c) $1\times$; (d) $0.05\times$. EPR conditions: temperatures as listed; frequency, 34.2 GHz; power, 0.09 mW (a,b); 0.009 mW (c,d); $B_{\text{mod}} = 0.1$ mT_{pp} at 100 kHz (a–c) or 0.4 mT_{pp} at 3.1 kHz (d).

centered at $g = 2$ with smaller, poorly resolved peaks (except hyperfine) extending out in either direction. The $S = 3, 4,$ and 5 manifolds each display one 11-line hyperfine pattern from one transition, but the position of the pattern depends on the spin state. The sum produces a spectrum which is dominated by those three spin manifolds, whose overlapping features produce a significantly broadened spectrum.

In the parallel mode, with increased temperature (Fig. 3d), the hyperfine pattern becomes more clearly defined as the $2|4$ transition no longer dominates the spectrum, which can be seen more clearly in the inset to Fig. 3. Again, the signals observed at high temperature result from overlapping features of the highest excited spin manifolds. In the parallel mode, the $\Delta M_S = \pm 2$ transitions are the origin of these overlapping features of the spectrum.

The sharp hyperfine patterns shown thus far are visible in samples prepared in neat DMF or DMF/acetonitrile mixtures. The observation of hyperfine also depends on the rate of freezing of the samples. Samples of **1** in DMF, frozen by plunging the EPR tube in to liquid nitrogen gave resolved hyperfine. Independent of the rate of freezing, samples prepared in neat acetonitrile (Fig. 6) show no Mn(II) dimer hyperfine patterns at any temperature. No change in lineshape was observed after a 10-fold sample dilution. The six-line hyperfine signal at $g = 2$ is from a mononuclear Mn(II) impurity of $<4\%$. Analysis of the spectra reveal that the molecular parameters are slightly changed in acetonitrile, as determined by the simulations overlaid on the data (dashed lines) and the parameters given in Table 1. We expect that different solvent interactions could result in subtle changes in \mathbf{D} , J , and \mathbf{r} . For the simulations, the value of r was fixed at the crystallographic Mn–Mn distance. The change in molecular parameters is most apparent from the low temperature spectrum (Fig. 6a) in which the signals arising from the two $\Delta M_S = \pm 1$ transitions now overlap at $g = 2.5$. For **1** in DMF, these transitions had g -values of 2.6 and 2.3 (Fig. 2a). Raising the temperature to 4 K (Fig. 6c) and then 50 K (Fig. 6d) causes new signals to appear in the spectrum from the higher excited spin manifolds, but none of these show any sign of Mn(II) dimer hyperfine. The parallel mode spectrum (Fig. 6b) shows only the signal from the $2|4$ transition at $g = 4.1$ which diminishes with increased temperature and shows no hyperfine lines. The loss of hyperfine resolution is not due to the small change in zero-field parameters, but can be attributed to an intermolecular interaction for **1** in (CH₃CN) (see Section 5).

4.2. X-Band EPR data of $[(Me_3TACN)_2Mn(II)_2(\mu-OAc)_3]BPh_4$ (**1**)

Figs. 7 and 8 show perpendicular and parallel mode X-band EPR spectra (solid lines) and simulations

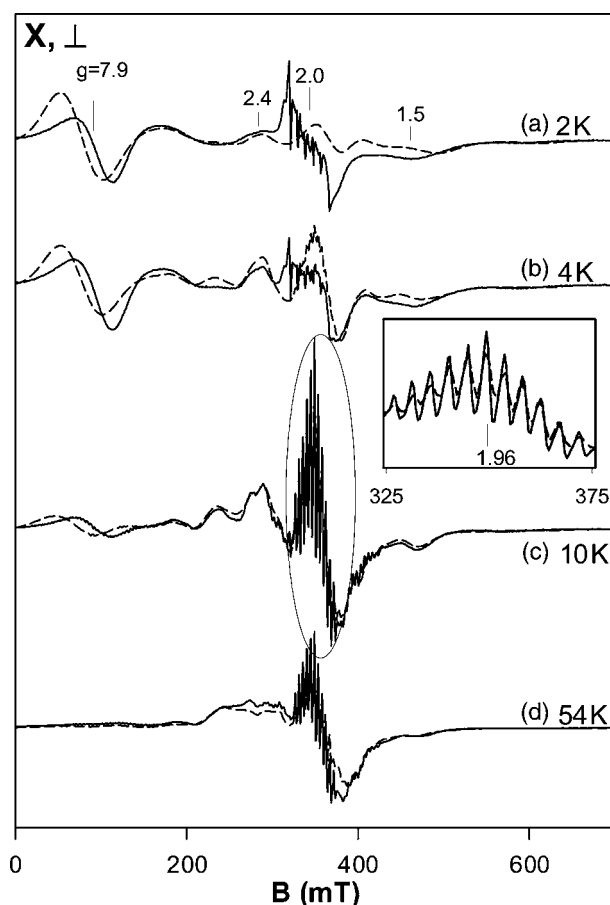


Fig. 7. Variable temperature, perpendicular mode, X-band EPR spectra (solid lines) and simulations (dashed lines) of an 11.5 mM sample of **1** in 50:50 CH₃CN:DMF. The simulation parameters are given in Table 1. Relative displayed intensities: (a,b) 1 \times , (c) 2 \times , (d) 3 \times ; EPR conditions: temperatures as listed; frequency, 9.62 GHz; power, 0.02 mW (a,b); 0.2 mW (c); 2 mW (d); $B_{\text{mod}} = 0.6 \text{ mT}_{\text{pp}}$.

(dashed lines) of **1** at various temperatures. X-band spectra of solid samples of **1** show similar but broader features without resolved hyperfine. The broadening is presumably due to intermolecular interactions and thus we have not analyzed the solid data in detail.

The simulations of the X-band spectra use the same parameter set as for Q-band, given in Table 1. To demonstrate which features grow in with increasing temperature, the simulations of each individual spin manifold are shown in Fig. 9 for both $B_1 \perp B$ and $B_1 \parallel B$. Fig. 7a shows the spectrum at 2 K for $B_1 \perp B$, in which the prominent feature is a large resonance extending towards zero field with a zero-crossing at $g = 7.9$. This signal arises from the $2|4$ transition of the $S = 1$ manifold. The six-line hyperfine signal is due to the same mononuclear Mn(II) impurity seen in the Q-band spectra. The $\Delta M_S = 1$ transitions, $2|3$ and $3|4$, observed in the Q-band spectrum, are so broadened at X-band that no significant features are observed. Fig. 8a shows the spectrum at 2 K for $B_1 \parallel B$, containing one large peak

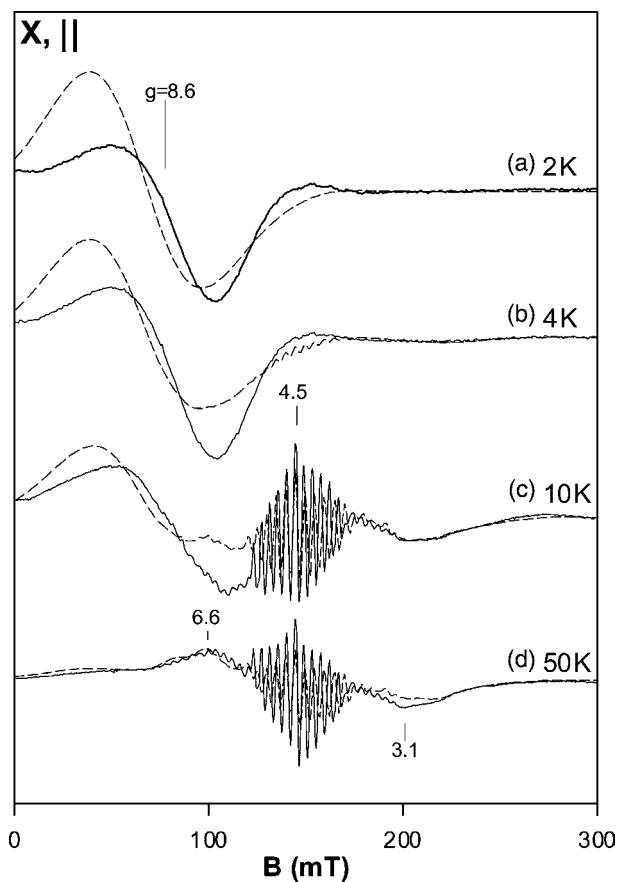


Fig. 8. Variable temperature, parallel mode, X-band EPR spectra (solid lines), and simulations (dashed lines) of an 11.5 mM sample of **1** in 50:50 CH₃CN:DMF. The simulation parameters are given in Table 1. Relative displayed intensities: (a–d) 1×; EPR conditions: temperatures as listed; frequency, 9.27 GHz; power, 0.002 mW (a–c); 0.2 mW (d); $B_{\text{mod}} = 0.6 \text{ mT}_{\text{pp}}$.

extending towards zero field with a zero-crossing at $g = 8.6$. As in the Q-band spectra, this feature has the same field position and lineshape as its perpendicular mode complement and also arises from the $2|4$ transition of $S = 1$.

The lineshape of the low field ($B < 150 \text{ mT}$, $g > 4.5$) transition at X-band in both perpendicular and parallel modes becomes distorted relative to that predicted by the simulations and the line position is slightly off. A similar line distortion has been observed previously for Fe(II) complexes and proteins [48]. The distortion of the signal lineshape is observed only near low field and is not due to unresolved hyperfine. We suspect that the distribution in the zero-field parameters may not be accurately modeled as a Gaussian distribution, but is perhaps skewed. Skewed distributions of zero-field parameters have been invoked previously for Fe³⁺ of myoglobin [46d]. In the low-field region, the resonance position is highly dependent on the zero-field splitting and thus deviations from a Gaussian distribution would be more evident. These same transitions are accurately

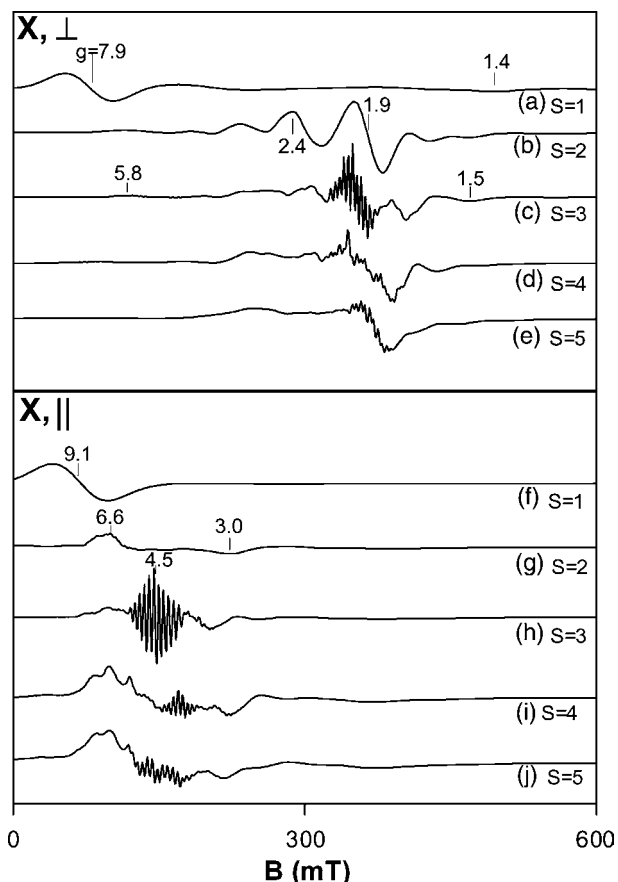


Fig. 9. Simulations of the individual spin manifolds $S = 1$ to 5 of complex **1** (a–e) for $B_1 \perp B$ (9.62 GHz) and (f–j) for $B_1 \parallel B$ (9.27 GHz); $T = 26 \text{ K}$. Simulation parameters are from Table 1. The relative displayed intensities are: (a) 10×; (b) 3×; (c–e) 1×; (f,g,i,j) 50×; (h) 25×.

simulated in the Q-band spectra where the resonance occurs at a higher magnetic field.

At 2 K, the other features in the $B_1 \perp B$ spectrum (Fig. 7a) between $g = 2.4$ and 1.5 are from the $S = 2$ manifold. Upon increasing the temperature to 4 K (Fig. 7b), the signals from the $S = 2$ manifold are more apparent, since the Mn(II) impurity signal has lower relative intensity. Unlike the signals arising from the $S = 1$ spin manifold, those visible from the $S = 2$ spin manifold originate predominantly from $\Delta M_S = \pm 1$ transitions. Similar to what was observed at Q-band, there are almost no discernable changes in the parallel mode spectrum upon raising the temperature from 2 to 4 K (Fig. 8b).

At a temperature of 10 K, the $S = 3$ manifold contains 10% of the spins and new resonances are observed for both $B_1 \perp B$ (Fig. 7c) and $B_1 \parallel B$ (Fig. 8c). Most prominent is the 11-line hyperfine pattern (4.6 mT spacing) which can be seen more clearly in the inset of Fig. 7 centered at $g = 1.96$. As in the Q-band spectrum, this hyperfine pattern results from a single $\Delta M_S = \pm 1$ transition ($12|13$), while the hyperfine lines of the other five $\Delta M_S = \pm 1$ transitions are unresolved. These five

$\Delta M_S = \pm 1$ transitions contribute predominantly to the peaks at $g = 3.0$ and 1.5 . As the temperature is increased, the perpendicular mode $2|4$ transition gradually disappears with the depopulation of the $S = 1$ spin manifold. Consequently, the $\Delta M_S = \pm 2$ transitions of the higher spin manifolds, which exhibit some hyperfine at $g = 5.8$, become more apparent in the spectrum. In the parallel mode spectrum (Fig. 8c) an 11-line hyperfine pattern at $g = 4.5$ can be seen quite clearly in the spectrum at 10 K. Again, as in the Q-band spectrum, this pattern arises from a single one of the four $\Delta M_S = \pm 2$ transitions ($12|14$) while the other transitions are unresolved.

At higher temperature, the spectral features become more broad and less well-defined due to population of the excited spin manifolds up to $S = 5$. The higher spin manifolds all have features in approximately the same field positions, clustering about $g = 2$, as seen in Fig. 9. At 54 K (Fig. 7d), the majority of the spectral intensity is centered around $g = 2$, with smaller peaks and shoulders extending away from this central feature in either direction. In the parallel mode spectrum, the signal from the $S = 1$ spectrum decreases in intensity with increasing temperature, while other spectral features become broadened and less well defined. At 50 K (Fig. 8d), the parallel mode EPR spectrum is dominated by the 11-line hyperfine pattern from the $S = 3$ manifold, and is flanked by features at $g = 6.6$ and 3.1 . These features originate from transitions from the $S = 2$ to 5 manifolds as shown in the simulations in Fig. 9. Above 50 K, the relative intensities and the sharpness of individual features change, but no new spectral features appear. As seen previously in the simulations of the Q-band spectra, the X-band perpendicular and parallel mode spectra of the various spin manifolds have features which cluster about a given field position. The splittings of the energy levels within a given spin manifold are dominated by the Zeeman term in the Hamiltonian, and so the $\Delta M_S = \pm 1$ transitions which give rise to the perpendicular mode spectra and the $\Delta M_S = \pm 2$ transitions which give rise to the parallel mode spectra all cluster about the same respective region of magnetic field.

4.3. Determination of the exchange coupling parameter J

The simulations shown in the above figures all fit the data quantitatively, consequently, the value of J is determined by the simulations. However, the task of simulating the spectra is simplified if an approximate value of J is known. The exchange coupling constant of **1** determined by magnetic susceptibility is $J = -1.7 \pm 0.1 \text{ cm}^{-1}$ [39]. Our first simulations attempts were based on this value, but as the work progressed we found better simulation fits with $J = 1.5 \text{ cm}^{-1}$. Independently, we also analyzed the temperature variation of the EPR intensity of four different signals originating from the

$S = 1$ and 3 manifolds. The $S = 1$ population was measured from the $\Delta M_S = \pm 2$ transition of this spin manifold ($2|4$). The corresponding EPR signals occur at $g = 4.1$ (Q-band, Fig. 6) and $g = 7.9$ (X-band, Fig. 7). These signals are sufficiently isolated from other resonances and their intensity as a function of temperature is shown in Fig. 10 (squares). The $S = 3$ signal intensity was measured as the peak-to-peak height of the resolved hyperfine lines which originate from this spin manifold. The intensity measurements are shown in Fig. 10 (triangles) for the hyperfine signals at $g = 4.1$ (Q-band, Fig. 3) and $g = 1.96$ (X-band, Fig. 7). Theoretical curves predicting the Boltzmann populations of each spin manifold are overlaid on the data, where each curve represents the total population of all energy levels within a given spin manifold. Population curves for all the spin manifolds of this system are included in Fig. 10 for completeness. From these data, we find an exchange coupling constant of $J = -1.5 \pm 0.3 \text{ cm}^{-1}$. This value of J is in agreement with that determined by the magnetization studies. The small value of J results in contributions to the EPR spectra from all excited spin manifolds at temperatures as low as 20 K. The simulations of the spectra of **1** in a 50:50, DMF:CH₃CN

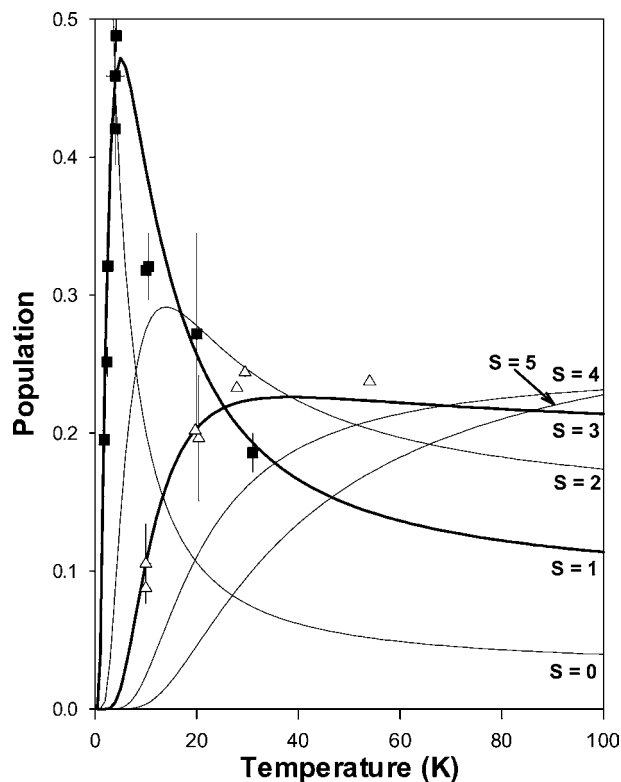


Fig. 10. Signal intensity times temperature as a function of temperature for complex **1**, for the signals at $g = 4.1$ (Q, $B_1 \perp B$) and $g = 7.9$ (X, $B_1 \perp B$) (squares), and for the hyperfine signals at $g = 4.1$ (Q, $B_1 \parallel B$) and $g = 1.96$ (X, $B_1 \perp B$) (triangles). The theoretical curves are the populations of the six spin manifolds of a Mn(II) dimer for $J = -1.5 \text{ cm}^{-1}$. The curves for the $S = 1$ and 3 manifolds (thick lines) align with the experimental data.

mixture use $J = -1.5 \text{ cm}^{-1}$, while those of the spectra in neat CH_3CN use $J = -1.7 \text{ cm}^{-1}$, each of which have been shown to match the respective experimental data well. The small change in the value of the exchange coupling may be due to the solvent-dependent changes in molecular parameters noted previously.

4.4. EPR spectroscopy of $(\text{Et}_4\text{N})_2[\text{Mn}(\text{II})_2(\text{salmp})_2]$ (**2**)

We have also studied the complex $(\text{NEt}_3)_2[\text{Mn}(\text{II})_2(\text{salmp})_2]$ (**2**) ($\text{NEt}_3 = \text{tetraethylamine}^{1+}$; $\text{salmp} = 2\text{-bis(salicylideneamino)methylphenolate}^{3-}$) in which the Mn(II) centers of the dimer are bridged by two phenoxide oxygen atoms provided by the chelating Schiff base ligands [38]. The X-band EPR spectra of **2** recorded at 2 K (dotted line) and at 6 K (solid line) are shown in Fig. 11a. The first observable features in the X-band spectra at low temperature arise not from the $S = 1$ manifold but from the $S = 2$ manifold. A simulation of the $S = 2$ manifold is shown in Fig. 11b. The feature at $g = 10.6$ is from a $\Delta M_S = \pm 2$ transition of $S = 2$ while the other spectral features at $g = 3.2$, 2.4 and 1.8 arise from $\Delta M_S = \pm 1$ transitions of the $S = 2$ manifold, as demonstrated by the simulation. The $S = 1$ spin manifold of complex **2** is essentially “EPR silent” at X-band frequencies in both perpendicular and parallel modes. As a comparison, complex **1** at low temperature shows a signal at $g = 7.9$ (Fig. 7a) similar to that of complex **2** at $g = 10.6$. While both of these resonances originate from $\Delta M_S = \pm 2$ transitions, the $g = 7.9$ signal of **1** is from the $S = 1$ manifold, whereas the $g = 10.6$ signal of **2** is from the $S = 2$ manifold. Without careful analysis of signals, the two signals might be mistaken as originating from the same spin manifold.

The $S = 1$ manifold of complex **2** does show signals at Q-band frequency. At 2 K (Fig. 11c, solid line), the $S = 1$ manifold has a resonance at $g = 5.3$ arising from the $\Delta M_S = \pm 2$ transition ($2|4$). The same transition also gives rise to a parallel mode signal (data not shown) at approximately the same field position as was similarly observed for complex **1**. When the temperature is raised to 7 K (Fig. 11d, solid line), signals from the $S = 2$ manifold begin to appear in the high field region. The most prominent features are observed between $g = 2.2$ and 1.75 , and are matched reasonably well by the simulation (dashed line). The simulation of the $\Delta M_S = \pm 2$ transition (dashed lines) matches the experimental data less well with increasing temperature. The origin of these temperature-dependent changes is not due to new signals from higher spin manifolds. We suspect the complications are due to complex aggregation and intermolecular effects which cause temperature-dependent broadening of the spectra. At present, these complications have not allowed complete simulation of the signals.

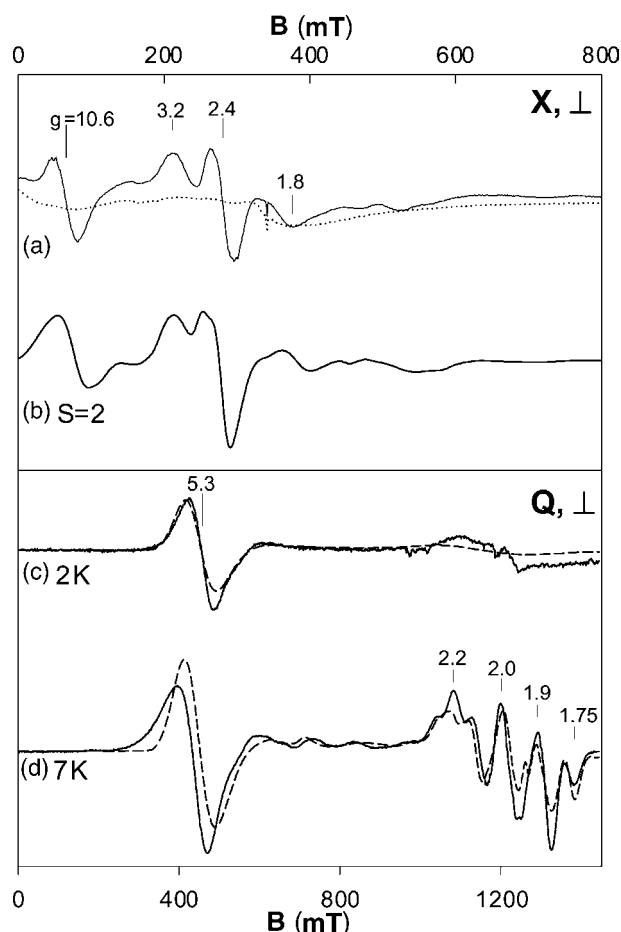


Fig. 11. (a) X-band perpendicular mode spectra of a 22 mM sample of $(\text{NEt}_3)_2[\text{Mn}(\text{II})_2(\text{salmp})_2]$ (**2**) in CH_3CN at 2 K (dotted line) and 6 K (solid line); (b) simulation of the spectrum arising from the $S = 2$ spin manifold; Q-band perpendicular mode spectra (solid lines) and simulations (dashed lines) of the same sample at (c) 2 K and (d) 7 K. The simulations are derived from simultaneous fits to X- and Q-band data taken over a range of temperatures. The parameters used for the simulations are: $D_{\text{Mn}} = 0.040 \text{ cm}^{-1}$; $\sigma_{D_{\text{Mn}}} = 0.012 \text{ cm}^{-1}$; $E_{\text{Mn}}/D_{\text{Mn}} = 0.428$; $\sigma_{E_{\text{Mn}}/D_{\text{Mn}}} = 0.148$; $r = 3.205 \text{ \AA}$; $\theta = 83^\circ$; $\phi = 196^\circ$; $A = 250 \text{ MHz}$; $J = -3.15 \text{ cm}^{-1}$; $g = 2$; $\sigma_B = 4 \text{ mT}$.

The exchange coupling parameter for **2** has not been previously determined. The intensity of the $g = 5.3$ signal was measured as the peak-to-trough height of this feature, giving a tentative determination of the exchange coupling parameter, $J = -3.15 \pm 0.25 \text{ cm}^{-1}$. A temperature-dependent magnetic field shift of the peak, as well as a temperature-dependent broadening, complicates this measurement. The determined J -value was corroborated by measurements of the temperature dependence of the $\Delta M_S = \pm 2$ transition from the $S = 2$ manifold of the X-band spectrum, but this signal begins to overlap with others from higher excited spin manifolds with increasing temperature. Nevertheless, it is clear that the bis-phenoxide bridge affords an anti-ferromagnetic exchange interaction between the Mn(II) ions.

5. Discussion

Dinuclear Mn(II) centers are often identified by observation of a characteristic 11-line hyperfine pattern. However, the origin of the pattern is uncertain and it is not observed for all dinuclear Mn(II) centers. The origin of the pattern is important because the intensity of the hyperfine lines is proportional to the population of the spin multiplet from which they originate, and a determination of J from the temperature dependence of this population is therefore dependent on the spin state assignment. In two previous studies of model complexes and proteins, the lowest multiplet to show the resolved hyperfine pattern has been assigned to the $S = 2$ state of the six spin manifolds, $S = 0$ to $S = 5$ [32,35]. For **1**, we find that lowest multiplet to show a resolved hyperfine pattern is the $S = 3$ state. The hyperfine lines are not resolved from the $S = 1$ and 2 states due to broadening of the lines by D - and r -strain (see below). As S increases, the effective zero-field splitting of an isolated multiplet decreases, consequently the effects of D -strain are diminished and the hyperfine lines are resolved for $S = 3$. The D -strain that we observe for **1** is large, but similar to that observed from Mn(II) substituted ribonucleotide reductase [11], and various Fe(II) complexes and proteins [48]. Although more work is needed to extend our findings to other Mn(II) complexes, the possibility that hyperfine is generally observed only for $S \geq 3$ must be considered.

The triple carboxylate bridge between Mn(II) ions in **1** gives an antiferromagnetic exchange interaction of $J = -1.5 \text{ cm}^{-1}$. Fig. 10 shows that more than one excited state is populated, even at low temperatures. For **2**, the bis-phenoxo bridge gives an exchange interaction of -3.2 cm^{-1} , and at temperatures above 7 K more than one excited state is populated. In previous studies of other dinuclear Mn(II) centers, the X-band EPR signals at lower temperatures have been assigned to the $S = 1$ and 2 multiplets. The characterization of complexes with EPR is usually based on these signals that roughly clustered around the $g = 2$ region and originate from the $\Delta M_S = \pm 1$ transitions of the various spin manifolds. However, the two complexes studied here demonstrate that the assignment of these signals to the $S = 1$ and 2 multiplets is questionable. The X-band spectra of the complexes studied here do not show significant signals from the $\Delta M_S = \pm 1$ transitions of the $S = 1$ state, due to extreme broadening of the resonances. The first significant signals clustered around the $g = 2$ region for complexes **1** and **2** in fact originate from the $S = 2$ and 3 multiplets. Without the benefit of simulations, incorrect assignments are possible, and consequently, an error in the determination of J .

In some of these previous studies of Mn(II) centers, the mathematical method of single-valued decomposition was utilized to identify the spectra arising from the

$S = 1$ and 2 states, and from their temperature dependence, arrive at a determination of J [32,33]. There are three notable difficulties with this method. First, the transition probabilities tend to increase with the increasing spin multiplicity. Thus, as shown in Figs. 5 and 9, signals arising from higher spin manifolds have greater relative intensities and tend to dominate even when populations of these manifolds are relatively low. Second, the signals from the many transitions of consecutive spin manifolds overlap in field position. The $S = 1$ spectrum can have no more than three transitions, and these transitions are often significantly broadened by D -strain, to give a rather featureless spectrum. Third, the assignment of features to the $S = 2$ spin manifold has relied on spectral diagrams calculated for axial symmetry [49], which likely do not apply to most Mn(II) proteins and model complexes. In addition, the diagrams predict only line positions and thus the analyses ignore relative intensity information. Using the parameters of various published deconvoluted $S = 1$ or 2 spectra, we have observed that our simulations differ significantly from the published spectra. If the $S = 1$ state produces broad featureless signals, the single-valued deconvolution procedure could mistakenly assign signals originating from the $S = 2$ and 3 states to $S = 1$ and 2 states, respectively.

Previous analyses of Mn dimer complexes have either detected or invoked the possibility of the phenomenon of exchange striction. This effect is observed when the metal–metal separation increases for each of the successive excited state spin manifolds [23,50]. The occurrence of exchange striction invalidates the standard exchange Hamiltonian ($-2JS_1 \cdot S_2$) used in Eq. (1). In addition, the zero-field splitting parameters, and the metal–metal dipolar energy may not be uniquely determined for each system spin manifold. This would justify the use of a different set of zero-field splitting parameters for each spin manifold which do not relate to a common set of parameters for the individual Mn(II) sites of the dimer. However, we have shown here for complex **1**, a single parameter set will simultaneously match all spectra at all temperatures. Moreover, a single value of the exchange coupling parameter J is appropriate for modeling the temperature dependence of signals from both the $S = 1$ and 3 spin manifolds. Thus, if exchange striction is present, it is not sufficiently large to be detectable.

Our new analytic method considers the spectra arising from all spin manifolds simultaneously in simulations of the experimental EPR spectra. The simulations are determined from a single set of parameters which are the intrinsic parameters of the individual uncoupled manganese sites (g , A , D , and E/D), the Mn–Mn distance, and the exchange interaction. The simulation program allows us to move beyond matching only the line positions, to include quantitative consideration of

the signal intensities and lineshapes. Therefore, this new method enables determination of the species concentration directly from the EPR spectra.

5.1. Broadening mechanisms of the EPR spectra

We have considered four independent broadening mechanisms for the prediction of resonance linewidths. The broadening effects do not occur uniformly across the spectral features. From spectra at various temperatures and frequencies, we can quantitatively determine the contribution to the linewidth from each broadening mechanism. This differs from previous phenomenological lineshape models which broaden lines with a uniform magnetic field-dependent parameter. A distribution of the orbital energy levels of the metal atoms will, through the spin–orbit interaction, cause a variation in the electronic spin energies of the metal from molecule to molecule in a sample. The origin of the distribution is believed to be variations of the metal–ligand bond lengths due to random solvent interactions. We characterize the spread in the electronic spin energies with Gaussian distributions in the parameters g , D , and E/D , which is referred to as g - [51] and D -strain [46]. The metal–ligand variations will also cause a variation in the Mn–Mn distance in the molecules of a sample. The spin energies also depend on the magnetic dipolar energy between Mn(II) ions (Eq. (2)), which is a direct function of the Mn–Mn distance. Consequently, the spin energies of the complex will also be distributed due to the variation in the Mn–Mn distance. This distribution is referred to as r -strain, and it will broaden resonances differently than g - and D -strain. We model r -strain with a Gaussian distribution in the Mn–Mn distance. Finally, at the lowest level of broadening effects are unresolved hyperfine interactions from ligands to the manganese which possess a nuclear spin. These hyperfine interactions are treated with a Gaussian distribution in the magnetic field at each resonance position.

At the lowest temperature, only the $S = 1$ manifold of complex **1** is populated. The broadening of resonances from the $\Delta M_S = \pm 1$ transitions is dominated by D -strain, whereas the $\Delta M_S = \pm 2$ transition is dominated by r -strain. The $\Delta M_S = \pm 1$ features in Q-band (Fig. 5a) are broad, and nearly vanish in X-band (Fig. 9a) due to D -strain. An illustration of this strain effect is given in Fig. 5a. The dashed line is a simulation of the $S = 1$ manifold with the same parameter set, except without D -strain. New peaks appear which are not resolved in the experimental data. A similar effect is observed for the $S = 2$ manifold except that the sensitivity to strain is less and the resonances sharpen. We have also considered the effects of g -strain on the spectra. The broadening from g -strain is highly field dependent, and thus the Q-band data would identify g -strain if present. Our data at two microwave frequencies could not be simultaneously

fit with g -strain, and thus this broadening mechanism does not make a significant contribution. This result is not surprising since the spin–orbit contributions to the g -value for Mn(II) are small.

The $S = 3$ manifold becomes populated at higher temperatures and now resolved hyperfine features are observed. The broadening of these and many of the $S = 3$ features is dominated by r -strain, which acts preferentially to broaden the hyperfine lines of most transitions. The dominant 11-line hyperfine pattern is due to one transition, as noted in Section 4. An illustration of the effect of r -strain is given in Fig. 5c. The dashed line is a simulation of the $S = 3$ manifold with the same parameter set, except without r -strain. All transitions now display resolved hyperfine, which is clearly not true of the experimental data. The resolution of the hyperfine pattern for a particular spin manifold is not critically dependent on the field anisotropy of the transition. For example, the $\Delta M_S = \pm 2$ transitions are isotropic but hyperfine lines are not resolved from these transitions of the $S = 1$ or 2 manifolds. Moreover, the anisotropic $\Delta M_S = \pm 1$ transitions (towards $g = 2.2$ and 1.8 in Fig. 5c) do show resolved hyperfine in the absence of r -strain. The magnitude of r -strain determined from the simulation of the data is $\sigma_r = 0.09 \text{ \AA}$. A value of σ_r less than 0.09 \AA results in resolved hyperfine features that are not apparent in the data. Values greater than 0.09 \AA give unreasonably broad hyperfine lines on the resolved signals. An independent assessment of the disorder in the Mn–Mn distance is available from the Debye–Waller disorder parameter of EXAFS spectroscopy. An EXAFS study of the complex $[\text{Mn}(\text{II})_2(\mu\text{-3-CIPhCOO})_2(\text{bpy})_4](\text{ClO}_4)_2$ found an Mn–Mn distance of 4.64 \AA with a disorder parameter of $\sigma = 0.08 \text{ \AA}$ [52]. EXAFS studies of dimeric Mn(II) centers in several proteins with carboxylate bridges found a range of values, $\sigma = 0.03$ to 0.2 \AA [53]. These values are consistent with that derived from EPR spectroscopy for complex **1**.

At higher temperatures, the $S = 4$ and $S = 5$ manifolds become populated, but the characteristic features from these manifolds are difficult to resolve from the lower spin manifolds. These manifolds also display one dominant 11-line hyperfine pattern that shifts in position depending of the spin state. Previously, the broadening of spectra and loss of resolution at higher temperatures was attributed to a combination of temperature-dependent broadening and zero-field splittings [34]. However, here we demonstrate that loss of spectral resolution can be attributed to overlapping of many signals as new manifolds become populated at higher temperature. These higher spin manifolds tend to cluster around $g = 2$, as shown in Figs. 5 and 9. This is a consequence of the lower effective zero-field splitting of the higher spin states (Eq. (6)), and energies of spin states which are then dominated by the Zeeman term of the spin Hamiltonian.

At the lowest level of broadening, the width is characterized by σ_B , which broadens resonances uniformly in magnetic field. For **1** in DMF we show simulations with $\sigma_B = 1$ mT, however our uncertainty in this number is fairly large; the value could be as low as 0.7 mT. This broadening we attribute to unresolved hyperfine splitting from the six N-atoms coordinated to the Mn(II). Under the assumption that the six ^{14}N atoms are equivalent, then the Gaussian distribution from an unresolved pattern of six equivalent $I = 1$ species will have a standard deviation of $\sigma_B \approx 3a_N$ where a_N is the hyperfine splitting (in mT) due to a single ^{14}N atom. Using $\sigma_B = 0.7$ mT, derived from simulation, gives $a_N = 0.23$ mT, or $A_N = 6.5$ MHz. There are few literature values of ^{14}N hyperfine constants for Mn(II) complexes. ESEEM spectroscopy of Mn(II) coordinated to the nitrogen of guanine [54] or NCS^- [55] found $A_N = 2.3$ and 2.7 MHz, respectively. The Mn–N distances for these complexes are not known and the Mn–N ligation is very different from that in complex **1**, thus a direct comparison is not possible. However, these values are reasonably consistent with our value of 6.5 MHz, and the conclusion that the unresolved broadening is due to the N-coordination of complex **1**.

The resolution of hyperfine lines is lost upon use of CH_3CN as a solvent. In fact, the presence of the hyperfine term is still evident in the spectra even though the lines are not resolved. The simulations of the spectra of the perpendicular mode in acetonitrile (Fig. 6), require inclusion of the isotropic hyperfine term with $A = 250$ MHz. Without this term, most of the linewidths of the features would be incorrect and result in poor simulations of the spectra. The hyperfine lines in the acetonitrile sample are in turn broadened by other molecular interactions which are not present for **1** in DMF. A complete match to the experimental data at both microwave frequencies for **1** in CH_3CN requires a significant increase in the magnetic field broadening parameter to $\sigma_B = 10$ mT. This value is far too large to attribute to unresolved ligand hyperfine splittings. The origin of this broadening can be attributed to a dipolar interaction between neighboring molecules, i.e., a through-space magnetic *intermolecular* interaction. We have calculated the magnetic field shift in the resonance position due to a neighboring Mn_2 molecule for such an interaction. An intermolecular distance of 10 Å between Mn_2 sites is sufficient to shift resonances by 10 mT, consistent with the observed increase in σ_B . We suspect this molecular aggregation can occur for **1** since this molecule presumably has a large electric dipole moment. Our attempts to minimize this aggregation by lowering the sample concentration had no effect. Extended networks of Mn(II) dimers have been observed in which the interdimer metal–metal distance ranges from 4.7 to 15.4 Å [56–59].

5.2. Magneto-structural correlations

The triply carboxylate bridged manganese dimer **1** has been previously characterized by X-ray crystallography and magnetic susceptibility [39]. The crystal structure of **1** reveals a metal–metal distance of 4.034 Å, which is typical of $\mu_{1,3}$ -carboxylate-bridged dimers, which range from 3.68 to 5.67 Å. The exchange constant $J = -1.5 \pm 0.3 \text{ cm}^{-1}$ is in the range of values for carboxylate-bridged Mn(II) dimers, $|J| = 0.2$ to 2.6 cm^{-1} [36,57,58,60–62]. The diphenoxide bridged complexes reported in the literature all have Mn–Mn distances within a narrow range of 3.30 to 3.42 Å (not including **2**). The range of exchange constants for this class is $+1.1 > J > -1.9 \text{ cm}^{-1}$ [29,56,63–65]. Complex **2** has shortest Mn–Mn distance (3.21 Å) for this class, and an exchange coupling determined here of $J = -3.2 \text{ cm}^{-1}$, which is the largest value for this class. The J -value for **2** is more negative than the range of literature complexes, which is consistent with the nearly 0.1 Å decrease in the Mn–Mn distance below the literature range.

As has been pointed out previously [37], various core bridging motifs for manganese dimers can be correlated to characteristic Mn–Mn distances. The exchange coupling constant is likely a complicated function of the metal–metal distance, which may allow for the possibility of metal–metal bonding, the type and number of the bridging ligands, and the bond angles between the metal atoms and the bridging ligands [66]. Correlations of J to a single structural parameter are difficult to make for the entire range of Mn(II) dimer core bridging motifs. Similar observations have been made for iron [67] and copper [68] dimers. In the case of Fe(III) oxo-bridged dimers, an exponential relationship to the parameter P has been observed, where P is a measure of the shortest exchange pathway in the dimer [67]. Our attempts to correlate J and P for the Mn carboxylate bridged dimers listed in the literature were unsuccessful. However, we did observe an approximate exponential relationship between the exchange interaction and the Mn–Mn distance.

The use of Eq. (1), with explicit inclusion of the dipolar coupling, allows a direct determination of the Mn–Mn distance and the orientation of the Mn–Mn vector relative to the **D**-tensor at a single manganese site. Thus, the relationship between \mathbf{r}_{MnMn} and the **D**-tensor at the individual metal sites is established. With this constraint, one would then like to determine the orientation of this individual manganese **D**-tensor relative to the molecular structure. The parameters given in Table 1 result in principal axis systems of the **D**-tensor which do not lie along the molecular bonds of **1**. We initially considered that a principal axis of the **D**-tensor might lie along the C_3 symmetry axis of **1**. For this case we would expect to observe spectra indicative of axial symmetry. However, the observation of strong $\Delta M_S = \pm 2$ transi-

tions for $S = 1$ indicates nonaxial symmetry. Moreover, quantitative analysis of the spectra indicate a significant value for E/D . We have not pursued analysis of the spectra of solid samples of **1** due to intermolecular broadening effects. Nevertheless, the solid spectra also show a large $\Delta M_S = \pm 2$ transition. The lower symmetry apparent in the EPR spectra is presumably due to small distortions of the molecule which are below the resolution of the crystallographic data. This is the first such determination for a Mn₂(II) complex and detailed structural correlations will require additional data from crystals and other complexes, which is not within the scope of the present paper.

6. Conclusions

We have developed a new primary method for the analysis of EPR of Mn(II) dimer systems. The spectra are simulated with a model which is fully quantitative and allows determination of Mn–Mn distances, zero-field splittings, and exchange couplings within the Mn(II) dimers. The spectral lineshapes are also treated quantitatively and the origin of the spectral broadening is determined. In particular, these new advances allow for the first time the determination of species concentrations directly from EPR spectra. This new approach should prove useful in future studies of electronic and structural properties of synthetic complexes and proteins.

Acknowledgments

This research was supported by a grant from the National Institutes of Health GM-49970 (M.H.). We thank Karl Wieghardt, Richard Holm, Thomas Weyhermüller, and Catalina Achim for their gifts of the samples studied here. We thank Doros Petasis and Caleb Culver for assistance in collecting the Q-band data.

References

- [1] S.V. Antonyuk, V.R. Melik-Adamyanyan, A.N. Popov, V.S. Lamzin, P.D. Hempstead, P.M. Harrison, P.J. Artymyuk, V.V. Barynin, *Crystallogr. Rep.* 45 (2000) 105–116.
- [2] V.V. Barynin, M.M. Whittaker, S.V. Antonyuk, V.S. Lamzin, P.M. Harrison, P.J. Artymyuk, J.W. Whittaker, *Structure* 9 (2001) 725–738.
- [3] Z.F. Kanyo, L.R. Scolnick, D.E. Ash, D.W. Christianson, *Nature* 383 (1996) 554–557.
- [4] R.S. Reczkowski, D.E. Ash, *J. Am. Chem. Soc.* 114 (1992) 10992–10994.
- [5] R. Cammack, A. Chapman, W.-P. Lu, A. Karagouni, R.P. Kelly, *FEBS Lett.* 253 (1989) 239–243.
- [6] C.G. Dismukes, *Chem. Rev.* 96 (1996) 2909–2926.
- [7] L. Zhang, M.J. Crossley, N.E. Dixon, P.J. Ellis, M.L. Fisher, G.F. King, P.E. Lilley, D. MacLachlan, R.J. Pace, H.C. Freeman, *J. Biol. Inorg. Chem.* 3 (1998) 470–483.
- [8] V.M. D'souza, S.I. Swierczek, N.J. Cosper, L. Meng, S. Ruebush, A.J. Copik, R.A. Scott, R.C. Holz, *Biochemistry* 41 (2002) 13096–13105.
- [9] T.A. Reiter, N.J. Reiter, F. Rusnak, *Biochemistry* 41 (2002) 15404–15409.
- [10] M. Högbom, M.E. Andersson, P. Nordlund, *J. Biol. Inorg. Chem.* 6 (2001) 315–323.
- [11] B.S. Pierce, T.E. Elgren, M.P. Hendrich, *J. Am. Chem. Soc.* 125 (2003) 874–875.
- [12] M.Y. Chae, G.A. Omburo, P.A. Lindahl, F.M. Raushel, *J. Am. Chem. Soc.* 115 (1993) 12173–12174.
- [13] B.C. Antanaitis, R.D. Brown, D. Chasteen, J.H. Freedman, S.H. Koenig, H.R. Lilienthal, J. Peisach, C.F. Brewer, *Biochemistry* 26 (1987) 7932–7937.
- [14] R.R. Poyner, G.H. Reed, *Biochemistry* 31 (1992) 7166–7173.
- [15] S.V. Khangulov, V.V. Barynin, V.R. Melik-Adamyanyan, A.I. Grebenko, H.V. Voevodskaya, L.A. Blumenfeld, S.N. Dobryakov, V.B. Ilyasova, *Bioorg. Khim.* 12 (1986) 741–748.
- [16] R.M. Fronko, J.E. Penner-Hahn, *J. Am. Chem. Soc.* 110 (1988) 7554–7555.
- [17] G.S. Waldo, R.M. Fronko, J.E. Penner-Hahn, *Biochemistry* 30 (1991) 10486–10490.
- [18] T.C. Brunold, D.R. Gamelin, T.L. Stemmler, S.K. Mandal, W.H. Armstrong, J.E. Penner-Hahn, E.I. Solomon, *J. Am. Chem. Soc.* 120 (1998) 8724–8738.
- [19] M.M. Whittaker, V.V. Barynin, S.V. Antonyuk, J.W. Whittaker, *Biochem* 38 (1999) 9126–9136.
- [20] J. Owen, *Suppl. J. Appl. Phys.* 32 (1961) 213S–217S.
- [21] G.L. McPherson, J.R. Chang, *Inorg. Chem.* 15 (1976) 1018–1022.
- [22] Y. Ishikawa, *J. Phys. Soc. Jpn.* 21 (1966) 1473–1481.
- [23] E.A. Harris, *J. Phys. C* 5 (1972) 338–352.
- [24] M.R. Brown, B.A. Coles, J. Owen, R.W.H. Stevenson, *Phys. Rev. Lett.* 7 (1961) 246–247.
- [25] E.J. Laskowski, D.N. Hendrickson, *Inorg. Chem.* 17 (1978) 457–470.
- [26] N. Kitajima, U.P. Singh, H. Amagai, M. Osawa, Y. Morooka, *J. Am. Chem. Soc.* 113 (1991) 7757–7758.
- [27] A. Hudson, M.J.G. Kennedy, *Inorg. Nucl. Chem. Lett.* 7 (1971) 333–336.
- [28] B. Mabad, P. Cassoux, J.-P. Tuchagues, D.N. Hendrickson, *Inorg. Chem.* 25 (1986) 1420–1431.
- [29] D.P. Kessissoglou, W.M. Butler, V.L. Pecoraro, *Inorg. Chem.* 26 (1987) 495–503.
- [30] Y. Gultneh, A. Farooq, S. Liu, K.D. Karlin, J. Zubieta, *Inorg. Chem.* 31 (1992) 3607–3611.
- [31] P.J. Pessiki, S.V. Khangulov, D.M. Ho, G.C. Dismukes, *J. Am. Chem. Soc.* 116 (1994) 891–897.
- [32] S.V. Khangulov, P.J. Pessiki, V.V. Barynin, D.E. Ash, G.C. Dismukes, *Biochemistry* 34 (1995) 2015–2025.
- [33] A.E. Meier, M.M. Whittaker, J.W. Whittaker, *Biochemistry* 35 (1996) 348–360.
- [34] B.E. Schultz, B.-H. Ye, X.-Y. Li, S.I. Chan, *Inorg. Chem.* 36 (1997) 2617–2622.
- [35] T. Howard, J. Telser, V.J. DeRose, *Inorg. Chem.* 39 (2000) 3379–3385.
- [36] K. Wieghardt, *Angew. Chem. Int. Ed. Engl.* 28 (1989) 1153–1172.
- [37] N.A. Law, M.T. Caudle, V.L. Pecoraro, in: A.G. Sykes (Ed.), *Advances in Inorganic Chemistry*, vol. 46, Academic Press, New York, 1999, pp. 305–440.
- [38] Y.B. Yu, C.-P. Wang, E.P. Day, R.H. Holm, *Inorg. Chem.* 30 (1991) 4067–4074.
- [39] K. Wieghardt, U. Bossek, B. Nuber, J. Weiss, J. Bonvoisin, M. Corbella, S.E. Vitols, J.J. Girerd, *J. Am. Chem. Soc.* 110 (1988) 7398–7411.

- [40] J.R. Pilbrow, *Transition Ion Electron Paramagnetic Resonance*, Clarendon Press, Oxford, 1990.
- [41] J.A. Weil, J.R. Bolton, J.E. Wertz, *Electron Paramagnetic Resonance: Elementary Theory and Practical*, John Wiley and Sons Inc, New York, 1994.
- [42] R.D. Dowsing, J.F. Gibson, M. Goodgame, P.J. Hayward, *J. Chem. Soc. (A)* (1969) 187–193.
- [43] R.D. Dowsing, J.F. Gibson, M. Goodgame, P.J. Hayward, *J. Chem. Soc. (A)* (1970) 1133–1138.
- [44] A. Bencini, D. Gatteschi, *Electron Paramagnetic Resonance of Exchange Coupled Systems*, Springer-Verlag, New York, 1990.
- [45] B.J. Gaffney, H.J. Silverstone, in: L.J. Berliner, J. Reuben (Eds.), *Biological Magnetic Resonance*, vol. 13, Plenum Press, New York, 1993, pp. 1–57.
- [46] (a) P. Eisenberger, P.S. Pershan, *J. Chem. Phys.* 47 (1967) 3327–3334;
(b) C. Mailer, C.P.S. Taylor, *Can. J. Biochem.* 50 (1972) 1048–1055;
(c) D.A. Hampton, A.S. Brill, *Biophys. J.* 25 (1979) 301–311;
(d) P.D. Levin, A.S. Brill, *J. Phys. Chem.* 92 (1988) 5103–5110.
- [47] D.T. Petasis, M.P. Hendrich, *J. Magn. Res.* 136 (1999) 200–206.
- [48] M.P. Hendrich, P.G. Debrunner, *Biophys. J.* 56 (1989) 489–506.
- [49] J. Baranowski, T. Cukierda, B. Jezowska-Trzebiatowska, H. Kozlowski, *J. Mag. Reson.* 33 (1979) 585–593.
- [50] G.L. McPherson, J.R. Chang, *Inorg. Chem.* 5 (1976) 1018–1022.
- [51] R.E. Anderson, W.R. Dunham, R.H. Sands, A.J. Bearden, H.L. Crespi, *Biochim. Biophys. Acta* 408 (1975) 306–318.
- [52] B. Albela, M. Corbella, J. Ribas, I. Castro, J. Sletten, H. Stoeckli-Evans, *Inorg. Chem.* 37 (1998) 788–798.
- [53] L. Stemmler, T.M. Sossong Jr., J.I. Goldstein, D.E. Ash, T.E. Elgren, D.M. Kurtz, J.E. Penner-Hahn, *Biochemistry* 36 (1997) 9847–9858.
- [54] S.R. Morrissey, T.E. Horton, C.V. Grant, C.G. Hoogstraten, R.D. Britt, V.J. DeRose, *J. Am. Chem. Soc.* 121 (1999) 9215–9218.
- [55] R. LoBrutto, G.W. Smithers, G.H. Reed, W.H. Orme-Johnson, S.L. Tan, J.S. Leigh Jr., *Biochemistry* 25 (1986) 5654–5660.
- [56] D. Luneau, J.-M. Savariault, P. Cassoux, J.-P. Tuchagues, *J. Chem. Soc. Dalton Trans.* (1988) 1225–1235.
- [57] H. Oshio, E. Ino, I. Mogi, T. Ito, *Inorg. Chem.* 32 (1993) 5697–5703.
- [58] J. Cano, G. De Munno, J. Sanz, R. Ruiz, F. Lloret, J. Faus, M. Julve, *J. Chem. Soc. Dalton Trans.* (1994) 3465–3469.
- [59] F. Nepveu, N. Gaultier, N. Korber, J. Jaud, P. Castan, *J. Chem. Soc. Dalton Trans.* (1995) 4005–4013.
- [60] I. Romero, L. Dubois, M. Collomb, A. Deronzier, J. Latour, J. Pecaut, *Inorg. Chem.* 41 (2002) 1795–1806.
- [61] C.-M. Che, W.-T. Tang, K.-Y. Wong, W.-T. Wong, T. Fong, *J. Chem. Res. (S)* 2 (1991) 30.
- [62] X.-M. Chen, Y.-X. Tong, Z.-T. Xu, T.C.W. Mak, *J. Chem. Soc. Dalton Trans.* (1995) 4001–4004.
- [63] D.J. Hodgson, B.J. Schwartz, T.N. Sorrel, *Inorg. Chem.* 28 (1989) 2226–2228.
- [64] M. Wesolek, D. Meyer, J.A. Osborn, A. De Cian, J. Fischer, A. Derory, P. Legoll, M. Drillon, *Angew. Chem. Int. Ed. Engl.* 33 (1994) 1592–1594.
- [65] H.-R. Chang, S.K. Larsen, P.D.W. Boyd, C.G. Pierpont, D.N. Hendrickson, *J. Am. Chem. Soc.* 110 (1988) 4565–4576.
- [66] U. Bossek, D. Nuhlen, E. Bill, T. Glaser, C. Krebs, T. Weyhermuller, K. Wieghardt, M. Lengen, A.X. Trautwein, *Inorg. Chem.* 36 (1997) 2834–2843.
- [67] S.M. Gorun, S.J. Lippard, *Inorg. Chem.* 30 (1991) 1625–1630.
- [68] R.W. Willet, in: R.D. Willet, D. Gatteschi, O. Kahn (Eds.), *Magneto-Structural Correlations in Exchange Coupled Systems*, D. Reidel Publishing Company, Boston, 1983, pp. 389–420.